

Effect of dynamic conditions on high-temperature corrosion of ternary carbonate salt for thermal energy storage applications

Luis González-Fernández ^{a,*}, Mikel Intxaustieta-Carcedo ^a, Oleksandr Bondarchuk ^b, Yaroslav Grosu ^{a,c,**}

^a Centre for Cooperative Research on Alternative Energies (CIC energiGUNE), Basque Research and Technology Alliance (BRTA), Alava Technology Park, Albert Einstein 48, 01510, Vitoria-Gasteiz, Spain

^b International Iberian Nanotechnology Laboratory, Av. Mestre José Veiga, s/n, 4715-330, Braga, Portugal

^c Institute of Chemistry, University of Silesia in Katowice, Szkołna 9 Street, 40-006, Katowice, Poland



ARTICLE INFO

Keywords:

Corrosion under dynamic conditions
Third generation concentrated solar power
Thermal energy storage (TES)
Molten salts
High-temperature
Eutectic ternary carbonate salt:
 $\text{Li}_2\text{CO}_3\text{-Na}_2\text{CO}_3\text{-K}_2\text{CO}_3$

ABSTRACT

$\text{Li}_2\text{CO}_3\text{-Na}_2\text{CO}_3\text{-K}_2\text{CO}_3$ salt is one of the candidates for 3rd generation concentrated solar power (CSP) plants, aiming to increase the operational temperature. This rise of temperature significantly increases the corrosion issue of molten salts. However, there is a lack of studies focused on the effect of salt flow on the corrosion kinetic for this ternary carbonate salt. In this work, corrosion experiments under static and dynamic conditions are compared for SS310 subjected to ternary carbonate salt at 600 °C.

A complete characterization of the corrosion layer, surface and cross-section, was carried out by means of SEM-EDX and XRD, while the molten salts after the corrosion tests were analysed by ICP-OES and XPS.

The dynamic experiment exhibited an enlarged spallation of the corrosion layer, leading to a thinner and less homogeneous scale. This feature exposed the chromium containing phase and considerably increased the extent of its dissolution into the salt. The obtained results remark that the detrimental effect of dynamic conditions on the corrosivity of molten carbonate salt cannot be neglected and must be taken into account in the design of 3rd generation CSP plants.

1. Introduction

Considering the global rise in the energy demand and the necessity of reducing the greenhouse gasses emission, renewable sources of energy have been promoted to increase their share in the electricity production. Among other renewables, concentrated solar power (CSP) technology is an essential element [1]. CSP technology redirects the solar energy to a heat transfer fluid (HTF) to increase its temperature, and this energy is transferred to a power cycle to produce electricity [2,3].

Although the levelized cost of electricity (LCOE) for photovoltaic (PV) technology is still lower than for CSP [4], one of the strengths of CSP technology is the feasibility and simplicity of incorporating a thermal energy storage (TES) system [5]. The incorporation of a TES system enhances the dispatchability of the CSP plant and reduces its LCOE [6,7].

The two-tank technology employing molten salt as thermal storage

media is the state-of-the-art for CSP plants that incorporate TES systems [8]. This technology has demonstrated its reliability and efficiency at industrial level in several CSP plants, such as Gemasolar, Cerro Dominador and Crescent Dunes. These plants employ a mixture of NaNO_3 and KNO_3 (60%–40% in wt%) as storage media, called solar salt. The compatibility of this salt with constructive materials has been extensively analysed in literature [9–15], because corrosion is one of the main issues regarding the use of molten salts as TES media at high temperature. Nevertheless, since these plants employ solar salt as storage media, their operation temperature range is limited to 565 °C. This limit reduces the overall efficiency of the plant in the solar-to-electricity conversion due to the steam Rankine thermodynamic cycle involved in the process.

To overcome this problem, next generation CSP plants are expected to replace the use of nitrate salts by other mixtures, to increase the working temperature [16]. The proposed candidates are chloride and

* Corresponding author.

** Corresponding author. Centre for Cooperative Research on Alternative Energies (CIC energiGUNE), Basque Research and Technology Alliance (BRTA), Alava Technology Park, Albert Einstein 48, 01510, Vitoria-Gasteiz, Spain.

E-mail addresses: lgonzalez@cicenergigune.com (L. González-Fernández), ygrosu@cicenergigune.com (Y. Grosu).

carbonate salts. Chlorides are more appealing in terms of price, but they present corrosivity issues [17]. Additionally, for synthesizing chloride salts, pre-treatments and/or further purifying processes might be needed [18,19]. On the other hand, carbonate salts are less attractive from the economic perspective, but to their advantages are lower corrosion and simple preparation method. Among other mixtures, the eutectic carbonate salt $\text{K}_2\text{CO}_3\text{-Na}_2\text{CO}_3\text{-Li}_2\text{CO}_3$ (34.5 wt%–33.4 wt% –32.1 wt%) is one of the most promising candidates for high temperature sensible thermal energy storage (HTSTES) material. This carbonate salt presents a moderate melting temperature (400 °C approx.) and extended thermal stability, up to 670 °C, 700 °C and >1000 °C in air, argon and CO_2 atmospheres respectively [20]. In addition, the K/Na/Li carbonate salt offers enhanced thermophysical properties compared to other molten salts: a heat capacity of $1.61 \text{ J}\cdot\text{g}^{-1}\cdot\text{K}^{-1}$, a thermal conductivity of $0.612 \text{ Wm}^{-1}\cdot\text{K}^{-1}$ and a density of 2.09 g cm^{-3} [21,22].

To check these promising features in a close-to-industrial level, an experimental pilot plant using this ternary eutectic carbonate has been designed, built and tested by Abengoa [23]. The aim was to test the performance of different components at high temperature in contact with carbonate salts. The authors point to the tank and pumps as the subsystems to be redesigned.

Although carbonate salts present lower corrosivity than that of the chloride mixtures, degradation of constructive materials is still an issue. Therefore, numerous studies analysing this aspect have been published. The influence of the temperature on the corrosion of SS316L and SS310S was confirmed by Lim et al. for Li/Na carbonates [24] and Frangini et al. for Li/K carbonates [25]. A porous corrosion layer of LiFe_5O_8 was formed below 600 °C, while a protective LiFeO_2 scale was found above that temperature. Lim et al. also analysed the effect of the CO_2/O_2 partial pressure [24], demonstrating that high CO_2 partial pressure hinders the formation of protective LiFeO_2 , while the partial pressure of O_2 presents no effect on the corrosion. Takeuchi et al. tested Fe–Cr alloys with variable Fe/Cr ratio by immersion corrosion tests in $\text{Li}_2\text{CO}_3\text{-K}_2\text{CO}_3$ mixtures at 650 °C under CO_2 atmosphere [26], showing that the alloy with highest Cr content has the best corrosion resistance. Besides, multi-layered corrosion scale was formed, with LiFeO_2 in the outer layer, LiCrO_2 in the inner layer and $\text{LiFeO}_2\text{-LiCrO}_2$ in the middle. A multi-layered corrosion structure was also presented by de Miguel et al. [27], for austenitic steel HR3C tested in eutectic ternary carbonate $\text{Li}_2\text{CO}_3\text{-Na}_2\text{CO}_3\text{-K}_2\text{CO}_3$ salt at 700 °C. The authors highlighted the incorporation of chromium to the molten salt. In this sense, Sah analysed the corrosion of SS304 in $\text{Li}_2\text{CO}_3\text{-Na}_2\text{CO}_3\text{-K}_2\text{CO}_3$ at 650 °C, and demonstrated that the dissolution of the corrosion products is a key parameter to assess the performance of a constructive material [28]. For the same carbonate salt mixture and temperature, Fernández et al. [29], reported the beneficial effect of incorporating aluminium in an alloy due to the formation of protective Al_2O_3 layer.

Several works concerning the corrosion of different constructive materials in eutectic mixture $\text{Li}_2\text{CO}_3\text{-K}_2\text{CO}_3\text{-K}_2\text{CO}_3$ at 450 °C were published by Sarvghad et al. [30–33]. The authors reported uniform corrosion morphology on the surfaces of SS316, duplex steel 2205 and carbon steel 1008, with no localized corrosion [30,31]. The cold-rolling of SS316L was proven to have little impact in the corrosion performances due to a dual role of the induced microstructural imperfections, such as grain boundaries and dislocation [32]. The initial stages were accelerated, with more areas of localized corrosion. However, the dislocations also facilitated the carbon diffusion and the subsequent carburization, which increased the corrosion resistance. Therefore, the overall corrosion rate remained unaffected. On the other hand, cold-worked Inconel 601 suffered localized attack, leading to relatively higher corrosion rate [33]. Though, the annealing of Inconel 601 resulted in a reduced corrosion rate with less localized attack areas. Moving to higher temperatures, Luo et al. evaluated the corrosion of SS316L in ternary $\text{Li}_2\text{CO}_3\text{-K}_2\text{CO}_3\text{-K}_2\text{CO}_3$ at 600 °C and 700 °C [34]. The authors reported a dual-structured corrosion layer formed by an initial oxidation of the components of the alloy and a subsequent lithiation,

followed by separation of corrosion products from the layer. Moreover, a severe corrosion was described at 700 °C, making inadvisable the use of SS316L without protective coating for applications at that temperature. Grosu et al. reported corrosion experiments in eutectic ternary carbonates for SS310 and SS347 at 600 °C [35,36]. The corrosion layer was composed of mixed oxides in a layered structure for both stainless steels, with the Cr containing phase located close to the substrate. Lithium was incorporated into the mixed oxides phases for SS310.

To summarize the presented works, in Fig. 1, the constructive materials employed for the corrosion experiments in molten carbonates are represented, together with the temperature of the test. The salt employed in these tests is eutectic ternary carbonate $\text{Li}_2\text{CO}_3\text{-Na}_2\text{CO}_3\text{-K}_2\text{CO}_3$, if not mentioned otherwise.

Unfortunately, most of the corrosion studies evaluating the effect of the molten salts are performed under static conditions. However, there are several elements where the movement of the salt plays an essential role in the degradation of materials, such as pipes, pumps, valves, heat exchangers, etc [37]. The published works reporting corrosion experiments under dynamic conditions are limited and mostly devoted to nitrate-based salt mixtures. García-Martín et al. [37] tested A516 carbon steel in solar salt at 500 °C and showed 50% increased corrosion rate compared to static conditions. Nieto-Maestre et al. [38] analysed the corrosion effect of solar salt-based nanofluid on A516 carbon steel and SS347 at 385 °C. Audigé et al. [12] examined the anticorrosion performance of two coatings, aluminide and nickel-aluminide, on P91 alloy at 580 °C in solar salt. The results for the uncoated P91 showed considerable mass gain in dynamic and static conditions, with significant spallation in both cases. After chemical etching of the corrosion layer, the metal mass loss rate demonstrated no difference between static and dynamic cases. For the same salt, Zhang et al. [39] also found a corrosion increase with dynamic conditions, by studying the influence of molten salt velocity on the corrosion behaviour of SS316 and SS321 at 565 °C. The authors presented an enhancement of the corrosion rates by increasing the salt flow velocity and stated that dynamic conditions increased the erosion and accelerated the dissolution on both stainless steels. Solar salt of both laboratory and commercial grades was used by Wang et al. [40] to assess the corrosion resistances of SS304 and SS316L, and nickel alloys 600 and 825 at 530 °C in static and dynamic

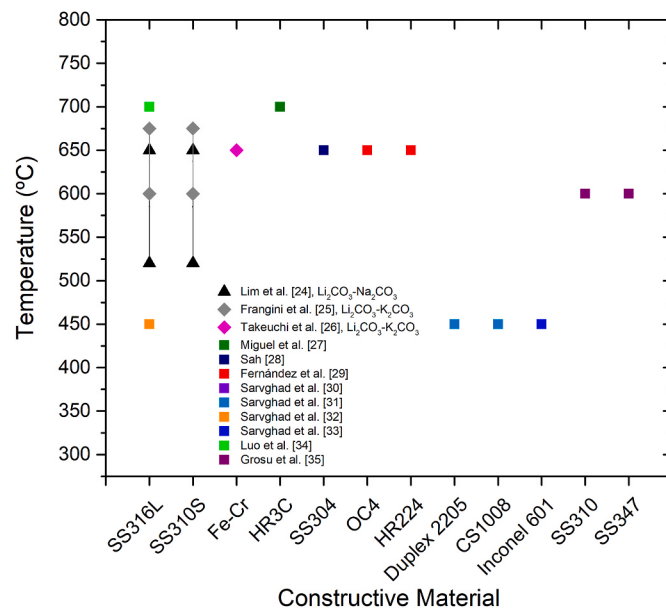


Fig. 1. Corrosion experiments reported in literature for carbonate salt mixtures. The alloys tested and the corresponding temperature of the corrosion test are represented. The salt employed in these tests is eutectic ternary carbonate $\text{Li}_2\text{CO}_3\text{-Na}_2\text{CO}_3\text{-K}_2\text{CO}_3$, if not mentioned otherwise.

conditions. In both cases, the ranking of corrosion resistance was SS304 < SS316L < 600 < 825, but more severe corrosion was demonstrated under dynamic state. Moreover, the commercial grade solar salt showed higher corrosiveness due to the presence of chloride ions. Similar results were obtained by Che et al. [41] for solar salt at 570 °C, with a corrosion resistance ranking in dynamic conditions of SS304 < SS316L < SS347H. A dynamic corrosion analysis in solar salt was conducted by Sutter et al. [42] for 2 ferritic alloys (430 and T91), 8 austenitic alloys (Sanicro25, 310 N, 316Ti, 316L, 321H, 15-15Ti, 347H, 347) and 4 nickel based alloys (Inconel 625, Haynes 230, Inconel 617 and HR6W) exposed to thermal cycles between 300 °C and 560 °C. The reported corrosion rates in dynamic conditions did not significantly differ for the ones in static tests.

In addition to the studies concerning solar salt, other salt mixtures based on nitrates were investigated by some authors. Fernández et al. [43] tested A516 carbon steel at 390 °C in a mixture of Na/Li/K nitrates. However, since the A516 was only exposed to dynamic conditions, without reference static test, no conclusions regarding the influence of the salt flow were extracted. On the contrary, the work of Ma et al. [44] analysed the corrosion of SS316L at 565 °C in $\text{Ca}(\text{NO}_3)_2\text{-KNO}_3\text{-NaNO}_3\text{-NaNO}_2$ for different fluid velocities, ranging from 0.6 to 2 m/s. The authors demonstrated that the corrosion weight loss and the corrosion depth increased with the flow rate.

Fig. 2 provides a summary of the reported dynamic corrosion experiments, where the temperature of the corrosion experiment and the salt mixture are specified.

Nevertheless, these results cannot be extrapolated to the carbonate salts, since their corrosivity is larger, and the higher working temperature also promotes the corrosion processes. In this sense, it seems that for the moment, there is only one work presenting a corrosion experiment in eutectic ternary carbonate salt, $\text{K}_2\text{CO}_3\text{-Na}_2\text{CO}_3\text{-Li}_2\text{CO}_3$, under dynamic conditions [45]. Concretely, coated and uncoated P91 alloy was tested at 650 °C. The authors found higher spallation of the corrosion layer in static conditions, while larger metal loss took place for dynamically tested P91.

Therefore, considering the lack of works addressing dynamic experiments with molten carbonate salts, the objective of this work is to determine the effect of the salt movement on the corrosion process for

the eutectic ternary carbonate salt, emulating the dynamic conditions that take place when the salt is pumped. For this purpose, both dynamic and static immersion tests in ternary $\text{K}_2\text{CO}_3\text{-Na}_2\text{CO}_3\text{-Li}_2\text{CO}_3$ salt at 600 °C were carried out for SS310 samples. The obtained results corroborate that dynamic conditions significantly increase the spallation of corrosion layer. This detachment removes the less adhered phases and exposes chromium containing scale, which increases its dissolution into the molten salt leading to at least twofold degradation rate.

2. Methods

2.1. Materials and preparation

Eutectic ternary carbonate salt was employed for the corrosion test: 34.5% K_2CO_3 - 33.4% Na_2CO_3 - 32.1% Li_2CO_3 (weight concentration). The components of the ternary salt were purchased from Sigma-Aldrich, with a purity ≥99.0%. Previously verified drying protocols were applied to ensure the absence of moisture in the salt [36]. Before mixing in the correct proportions, the carbonates were dried at 120 °C in the oven for no less than 12 h. Afterwards, they were weighted and blended.

The samples and the rods, used to transmit the rotational movement from the engine to the sample, were prepared of SS310. The chemical composition of this stainless steel is detailed in Table 1.

As it can be seen in Fig. 3e, cross-shaped samples with 4 petals were employed in the tests. The samples were cut from a SS310 sheet having 2 mm thickness. The total length of the cross was approximately 70 mm, while the size of the 4 square-shaped petals was 22 mm. In order to facilitate the analysis of the samples after the corrosion test by separating the 4 petals of the cross, the junction between each petal and the central region was reduced to 6–7 mm. A central hole was bored and threaded in the sample to attach it to the rod by screwing.

Table 1
Chemical composition (wt%) of tested SS310.

Element	Fe	Ni	Cr	Mn	Si	P	C	S
Stainless steel 310	Balance	19.1	24.9	1.81	0.64	0.03	0.05	0.01

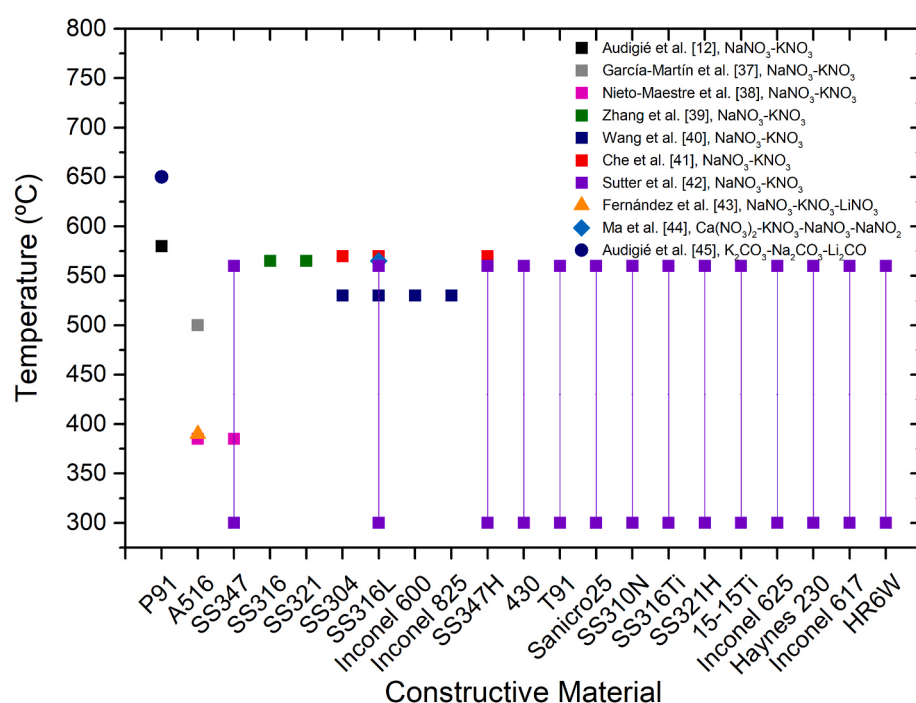


Fig. 2. Corrosion experiments reported in literature addressing dynamic conditions. The alloy tested, the temperature of the study and the salt mixture are specified.

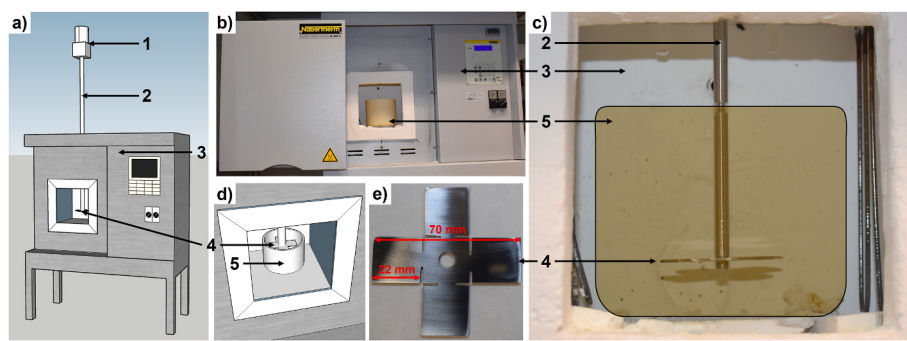


Fig. 3. Experimental setup for dynamic corrosion tests: schematic view (a, d) and photos (b, c, e) of electric motor (1), rotation-transmitting rod (2), furnace (3), SS310 sample (4), and alumina crucible (5).

Both surfaces of the samples were polished up to 1200 SiC sandpaper using ATM Saphir stationary polishing machine. Next, the samples were successively cleaned in acetone, ethanol and distilled water in an ultrasonic bath for 15 min for each solvent.

2.2. Corrosion protocol and experimental setup

For carrying out the dynamic test, a dedicated setup was developed - Fig. 3.

The movement is produced by an electric motor located above the furnace and connected to the SS310 rod by a Teflon junction. Teflon was chosen to avoid any electrical connection between the sample and the motor that could have an influence on the corrosion process. The rod enters into the furnace through a hole in its top part. The bottom extreme of the rod is threaded in the way that the sample can be attached by screwing. With this configuration, spinning the sample intends to mimic the dynamic corrosion conditions produced in the inner walls of pipes due to molten salt pumping.

During the test, since the SS310 sample was screwed to the rod, the rotation without touching either the wall or the bottom part of the alumina crucible was ensured. A total mass of 685 g of carbonate salt was employed to ensure that the samples were completely immersed during the experiment.

The test was carried out at a spinning rate of 60 rpm, which means a linear velocity of ~ 0.2 m/s in the central part of the petals. This velocity is comparable to the range of fluid velocities near to pipe bends and valves in the CSP plants, 0.2–0.5 m/s [12,37,45]. To ensure that the results were not influenced by a difference in the salt velocity, the analysis were restricted to the region of the petals that corresponds to a linear velocity of (0.20 ± 0.02) m/s. Especially for the cross-section characterization.

When the setup was completely assembled, the furnace was heated to 450 °C in air atmosphere with 5 °C/min heating rate and without rotating the sample. Then, 1 h in isothermal conditions was maintained to ensure that salt entirely melts. Later, the salt was heated to 600 °C at the same heating rate. When the desired temperature was reached, the motor was turned on and the temperature was maintained for 600 h, followed by a cooling step to 450 °C at 5 °C/min and recovery of the sample while the salt is in the molten state.

After conducting the corrosion test under dynamic conditions, another study was carried out with the same experimental configuration but without rotation of the sample. For the test in static conditions, new cross-shaped sample and new rod were prepared, as well as fresh ternary carbonate mixture. The aim of this static experiment is to serve as a reference test for assessing the effect of dynamic conditions on the corrosion process.

The 4 petals of the samples tested in dynamic and static conditions were cut to separate them from the central part for detailed characterization. In this way, 4 samples of each corrosion test were available. Afterwards, the remaining salt was cleaned with distilled water.

2.3. Characterization techniques

2.3.1. Scanning electron microscopy - SEM

For the SEM analysis, a Quanta 200 FEG model was used in high vacuum mode at 20 kV with backscattered electron detector (BSED) and Everhart-Thornley detector (ETD). Energy-Dispersive X-Ray spectroscopy (EDX) was performed for elemental mapping.

Firstly, the surfaces of all the samples were analysed by both sides. Secondly, the cross-section of samples was checked to analyse further the corrosion layer. For this purpose, the samples were imbedded in a resin holder composed of Aka-Resin and Aka-Cure catalyst (1 ml–0.135 ml proportion respectively). When the resin solidifies, it creates a hard shell that protects the corrosion layer from detaching during the cutting and polishing processes. The samples were cut using a Struers Miniton precision cutting machine, equipped with a diamond blade. To properly observe the samples' cross-section, they were polished successively with 240, 400, 800, 1200 and 2500 SiC sandpaper using ATM Saphir stationary polishing machine and distilled water as polishing fluid. In this sense, Lippiatti et al. [46] remarked the importance of sample preparation for SEM analysis and presented a preparation technique that allows the study of the cross-section of samples without removing or disturbing the metal-salt interface.

To determine the average corrosion layer thickness of the samples after the experiment, the cross-section SEM images were analysed by ImageJ software. The thickness of the corrosion scale was measured for more than 300 points to get a good statistic and a representative average thickness value.

2.3.2. X-ray diffraction - XRD

The X-ray diffraction measurements were carried out by means of a Bruker D8 Discover X-ray diffractometer equipped with a LYNXEYE detector using CuK α 1 radiation ($\lambda = 1.5418$ Å) in Bragg-Brentano 0:20 geometry. The data collection was carried out at room temperature, between 10 ° and 80 ° with a step size of 0.02 ° and a collection time of 1 s/step. Later, the phase identification of each sample was performed by EVA software.

2.3.3. Inductively coupled plasma optical emission spectroscopy – ICP-OES

Samples were analysed using a Horiba Ultima 2 (Jobin Yvon, Longjumeau, France) in conjunction with a AS500 autosampler and Activanalyst software (version 5.4).

The ICP-OES operating conditions were as follows: 1.0 kW of RF power, 13 l/min of a plasma-gas flow rate, 0.2 l/min of a sheath-gas flow rate and 0.25 l/min of a nebulizer-gas flow rate. Solutions were introduced into the plasma torch using nebulizer and a cyclonic type spray chamber at a flow rate of 0.87 ml/min.

A multi-elemental standard solution of 100 mg/l containing 25 elements supplied by Scharlab (Barcelona, Spain) was used for calibration. HNO₃ 69% from Scharlab (Barcelona, Spain) analytical grade and Ultrapure Water from Fischer Scientific (Waltham, Massachusetts, USA)

were used for dilutions.

The analytical wavelengths used for the measurements are listed in Table 2.

Concentrations of elements were quantified using five-point external calibration curves within the concentration range of 0.001–20 mg/l.

2.3.4. X-ray photoelectron spectroscopy characterization – XPS

The XPS measurements were performed in an ultra-high vacuum (UHV) system ESCALAB250Xi (Thermo Fisher Scientific). The base pressure in the system was below $5 \cdot 10^{-10}$ mbar. The XPS spectra were acquired with a hemispherical analyzer and a monochromated X-ray source (Al K α radiation, $h\nu = 1486.6$ eV) operated at 15 keV and 200 W power. The XPS spectra were recorded with pass energies 20 eV and 200 eV for high resolution and survey spectra, respectively. The spectrometer was calibrated by setting the Au 4f7/2 level to 84.0 eV measured on a gold foil.

XPS spectra were peak-fitted using Avantage data processing software. For peak fitting the Shirley-type background subtraction was used. Quantification was done using elemental sensitivity factors provided by the Avantage library.

The XPS system features a dual mode Ar ion source MAGCIS (Thermo Fisher Scientific) which can operate in monoatomic and cluster modes. The samples' surfaces before XPS characterization were cleaned by using Ar cluster ions of 1000 atoms. For Ar cluster cleaning an accelerating voltage of 4 keV was used. For depth profiling the MAGCIS was operated in the monoatomic mode with beam energy 4 keV and beam current 3 μ A.

3. Results and discussion

The state of the samples after the corrosion tests is shown in Fig. 4, for both static and dynamic conditions. It is clearly observed that both types of samples present a significant extent of spallation.

An image of the cross-shaped sample tested without rotation, just after being extracted from the furnace, is presented during the solidification of the remaining carbonate salt (Fig. 4a). Its counterpart tested under dynamic conditions (Fig. 4b) appears to be smoother, which seems to be due to more efficient detachment of the corrosion scale caused by the rotation. Images of one of the petals of the cross after cutting and cleaning are also shown for the static (Fig. 4c) and dynamic (Fig. 4e and f) tests. The 4 pieces obtained from the sample were separated before the cleaning process, to avoid as much as possible the loss of the oxide layer during the cutting, since it was obvious that there were corrosion products partially attached to the samples. For the static samples, the last step was to remove the loosely stuck corrosion scale, to analyse it separately. One piece after the removal of the scale is presented in Fig. 4d.

The analysis of samples surface by SEM evidences the difference between dynamic and static cases (Fig. 5). The precursor of the large spallation observed in dynamic test is demonstrated in Fig. 5b, as a kind of bubbles in the corrosion layer with the top broken. In the regions where the layer is already detached, sign of these formations can be detected. However, a completely different morphology is appreciated

for the samples tested in static conditions (Fig. 5a), where three stacked layers are present. While the crystals formed during the process in top and bottom layers are big enough to be distinguished even for the lowest magnification (Fig. 5a), the middle layer is composed of smaller crystals. Thus, the middle level presents a more regular and smoother topology. On the contrary, protuberances are visible in the bottom layer. The higher magnification images correspond to the region of corrosion layer well attached to the metallic matrix, below the spalled scale. While the sample in static conditions presents bigger octahedral crystals (Fig. 5c), the formations of the dynamic test are smaller and with more disordered shape (Fig. 5d). This difference is attributed to the salt flow, that hinders the formation of bigger crystals, whereas in the static experiment the growth of the oxides is promoted.

The radical difference in the spallation nature of each case is even more evident in Fig. 6, where cross-section SEM micrographs are presented. Although both samples had been subjected to the exact same conditions (temperature profile, test duration, experimental configuration, etc.), the thickness of the attached corrosion layer is remarkably different depending on dynamic/static conditions. The unique reason that can explain this effect is that the rotation of the sample forces the detachment of the formed corrosion layer once it reaches certain thickness, due to a lack of adherence. During the static test, although there is some extent of spallation, the corrosion layer grows thicker since it is not eroded by the salt flow.

According to the corrosion layer thickness, the average corrosion rate for the static conditions was found to be $466 \pm 3 \text{ }\mu\text{m/year}$. There was some fluctuation of the corrosion layer thickness, resulting in a maximum corrosion rate of $668 \text{ }\mu\text{m/year}$ and a minimum rate of $364 \text{ }\mu\text{m/year}$. For the dynamic conditions such analysis was not possible due to the pronounced spallation. It should be noted that, while the obtained corrosion rate is within the limits of the previously reported data (between $73 \text{ }\mu\text{m/year}$ and $438 \text{ }\mu\text{m/year}$ [28,29]), one can notice that the average corrosion rate is noticeably higher in this work, while the deviation is much lower: $466 \pm 3 \text{ }\mu\text{m/year}$ measured in this work versus $157.0 \pm 41.5 \text{ }\mu\text{m/year}$ reported previously [28,29]. This points to reduced spallation, thus leading to more homogeneous corrosion layer thickness, in this work. The described differences can be attributed to a different salt mass-to-stainless steel superficial area ratio. In Refs. [35, 36], SS310 pieces with approximately 1000 mm^2 of external area were immersed in 5 g of salt. However, in the present work, 685 g of ternary carbonate salt were employed for testing a sample with an overall external surface of roughly 7000 mm^2 . This means that the salt to metal ratio of this test is 20 times higher than in Refs. [35,36]. Therefore, we highlight here the importance of salt-to-stainless steel ratio, which will be systematically studied in the upcoming work.

The XRD patterns of samples tested in static and dynamic conditions are plotted in Fig. 7. For the static experiment, both the diffractograms of the SS310 coupon after the corrosion test as well as the oxide scale barely attached and removed from the metallic piece are included. The pattern of the pristine SS310 is included in the Fig. 7 as a reference. The samples subjected to dynamic conditions, present a corrosion layer composed of mixed oxides, namely LiCrO_2 and $\text{Li}_{1.05}(\text{Fe},\text{Ni})_{0.95}\text{O}_2$, with higher presence of the Li–Cr compound. Due to the thin corrosion layer,

Table 2
Analytical wavelengths used for the ICP-OES measurements.

Element	Al	As	Ba	Be	Bi	Ca	Cd	Co	Cr
Wavelength (nm)	396.152	193.695	413.066	249.454	190.178	317.933	226.502	238.892	267.716
Element	Cu	Fe	K	Li	Mg	Mn	Mo	Na	Ni
Wavelength (nm)	327.396	259.940	769.896	670.784	279.079	257.610	204.598	589.592	216.556
Element	Pb	Se	Sr	Ti	Tl	V	Zn		
Wavelength (nm)	283.306	196.026	216.596	336.121	190.800	310.230	206.191		

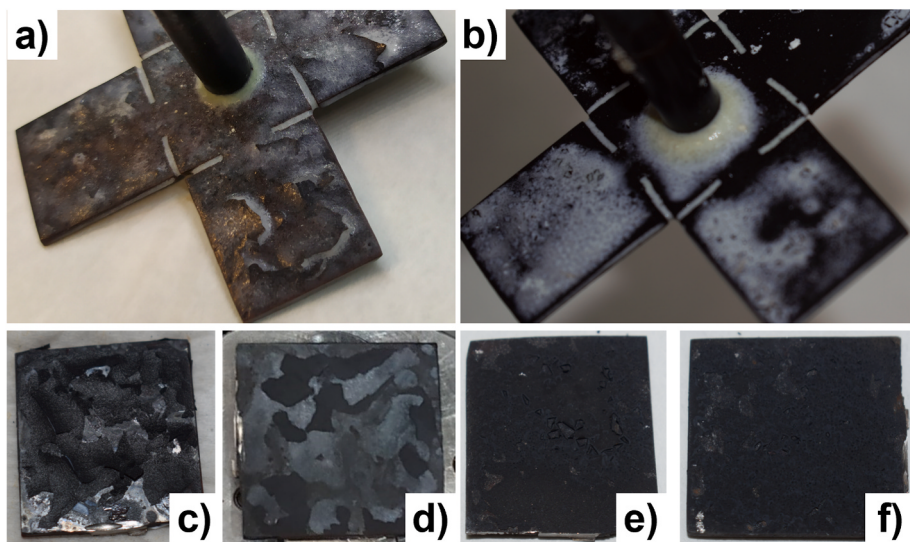


Fig. 4. Photos of the SS310 samples after 600 h corrosion experiment at 600 °C under static (a, c, d) and dynamic (b, e, f) conditions: just after the corrosion test (a, b), after separating and cleaning of the petals (c, e, f) and after removing the loosely attached corrosion scale (d).

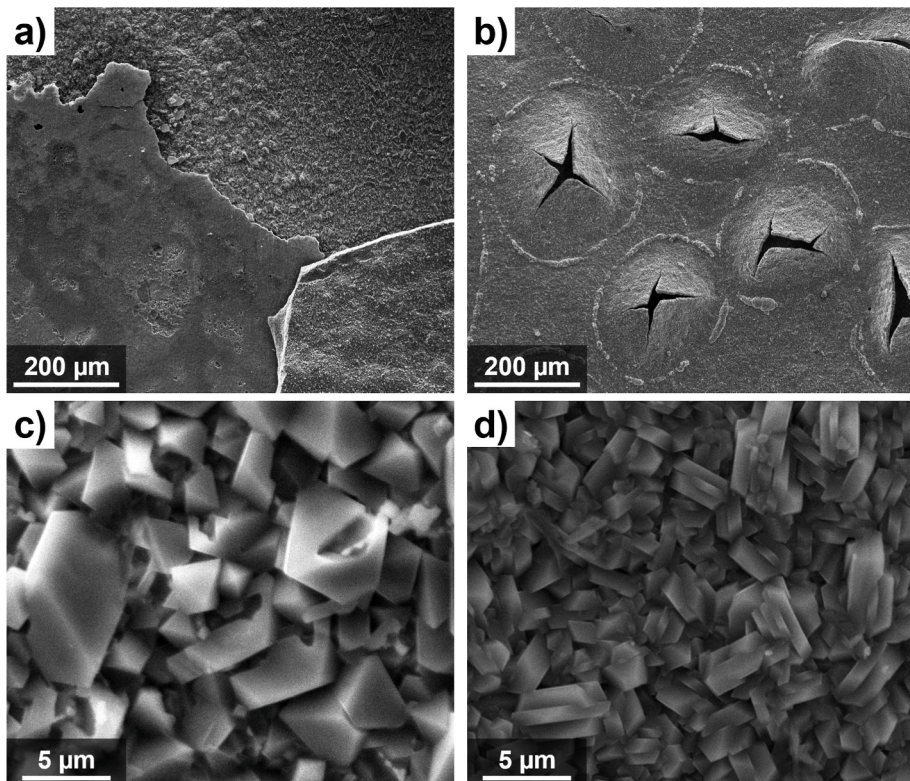


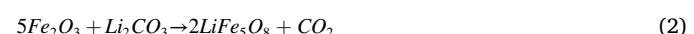
Fig. 5. SEM images of the SS310 samples after 600 h corrosion experiment at 600 °C under static (a and c) and dynamic (b and d) conditions.

one can observe the peaks corresponding to the pristine SS310 formed by cubic phases of Fe, Ni and Cr.

The static test samples, in addition to the abovementioned phases, present iron oxide, Fe_2O_3 , other mixed oxides such as $\text{Li}(\text{Fe},\text{Ni})_5\text{O}_8$ and MnNi_6O_8 ; as well as a minor contribution of K_2NiO_2 . Since the corrosion layer is significantly thicker in this case, the peaks of pristine SS310 do not contribute to the diffractogram. It is worth to mention that the corrosion layer formed during the static test demonstrates higher presence of iron oxides than the dynamic case. This may be attributed to a weaker adhesion of the Fe/Ni oxides, which leads to their removal upon dynamic test. This can be supported analysing the XRD results obtained

for the corrosion sheet removed from the static piece, since it is formed by the same compounds found attached to the metallic piece, except the Li–Cr mixed oxide. This means that there is no chromium containing oxide in the removed scale.

The formation of the Li–Fe mixed oxides, LiFeO_2 and LiFe_5O_8 , can be described according to the reactions (1) and (2) [36], while the Li–Cr oxide, LiCrO_2 , is produced according to reaction (3) [34].



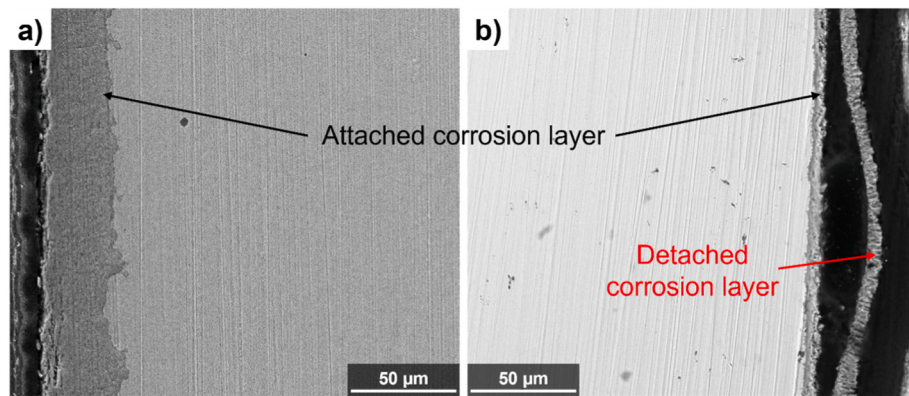


Fig. 6. SEM images of the cross-section of the SS310 samples after 600 h corrosion experiment at 600 °C for a) static and b) dynamic test.

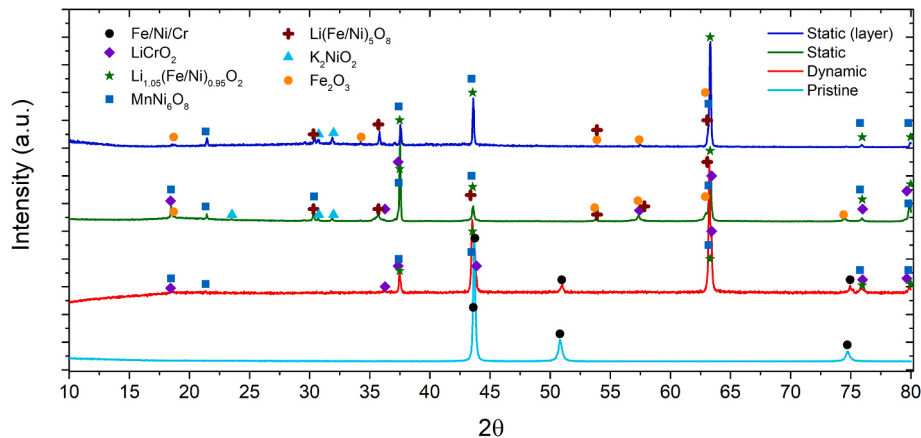


Fig. 7. XRD patterns of samples after 600 h corrosion experiment at 600 °C for static (piece and removed layer) and dynamic test (piece). Pristine SS310 is included as reference.



Combining the XRD results with the SEM-EDX analysis of the cross section, it can be stated that, in the sample tested in dynamic conditions (Fig. 8b), the LiCrO₂ phase is located below the Fe/Ni containing oxide, Li_{1.05}(Fe,Ni)_{0.95}O₂. This behaviour was previously reported for SS310 tested in carbonate salt in static immersion configuration [36]. Moreover, for static immersion corrosion test of SS316L with ternary K/Na/Li carbonate, phase stratification was found in the formed corrosion layer, but with different respective location [34]. In the SEM image, it can be seen that the outer region of the corrosion layer is already detached, although it is not completely separated because it is being held by the

resin (Fig. 8b). In that scale, there is no Cr and the Ni content is very scarce, indicating that it is mainly composed of Li_{1.05}Fe_{0.95}O₂.

In the static case (Fig. 8a), chromium is present all over the corrosion layer, not just in the interface between metallic piece and corrosion scale. Moreover, the Cr concentration is higher in the outer part of the corrosion layer, where Ni content is reduced. This indicates that Cr diffuses from the substrate to the corrosion layer. Such diffusion can be the reason for high concentration of Cr at the interface between the SS310 and corrosion layer under dynamic condition (Fig. 8b). Thus, the dynamic conditions can enhance Cr dissolution not only due to higher local gradient of Cr concentration between molten salt and SS310, but also due to thinner corrosion scale as a result of pronounced spallation.

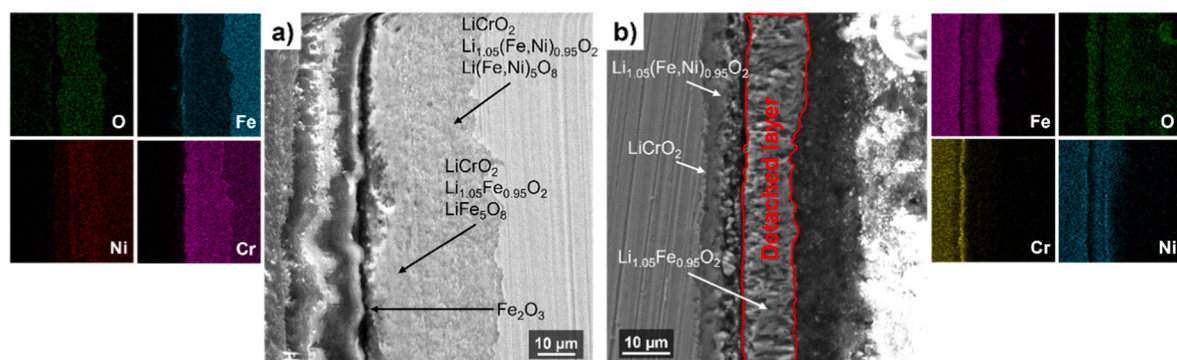


Fig. 8. SEM images and EDX-mapping of the cross-section of the SS310 samples after 600 h corrosion experiment at 600 °C under a) static and b) dynamic conditions.

Indeed, the loosely attached corrosion scale that was removed before analysing the static piece contained no chromium oxide.

The high iron concentration observed at the exterior part of the corrosion layer in Fig. 8a can be attributed to the Fe_2O_3 phase. The location of iron oxides in the outer part of corrosion layer has been previously reported [34], being in that case Fe_2O_3 and Fe_3O_4 .

It is worth mentioning that lithium is not detectable by SEM-EDX device and that manganese mapping was not acquired since Mn and Cr signals overlap.

For the sake of clarity, in Fig. 9, a scheme of the corrosion layer formed in static and dynamic conditions is represented. The figure presents the locations of the main oxide phases inside the corrosion scale, determined by the combination of XRD and SEM-EDX analyses.

Considering the location of each phase in the corrosion layer, and its continuous spallation during the dynamic experiments, when the Fe/Ni oxides are removed, the LiCrO_2 gets exposed to the carbonates salt, leading to its dissolution. In the static tests, since the detachment is less pronounced, the extent of the dissolution is lower. Another reason for having higher Cr dissolution level for dynamic conditions is that, due to the larger spallation and the flow of the salt, the chromium containing phase is in contact with fresh salt all the time, increasing the Cr concentration gradient compared to the static conditions.

The dissolved chromium oxide, Cr_2O_3 , produces a greenish colour of the salt, as it is observed in Fig. 10. It can be seen that the colour change of the salt is evident for both dynamic and static conditions, since initially the carbonate salt is white. However, one can see that not only intensity but the colour itself is different for the two cases. This difference may be due to the presence of reddish Fe_2O_3 phase in the static case as described above. In order to quantify the difference between static and dynamic conditions, ICP techniques were applied to the salts after both tests.

The presence of chromium as well as other contaminants or impurities in the salts after the corrosion experiments has been confirmed by means of ICP analysis. The results of the ICP-OES study are included in Table 3. The concentration of Cr in the salt used in the dynamic experiment is more than twice the one of the static test. This is in agreement with the higher exposure to dissolution of LiCrO_2 due to the spallation. Considering the lack of adherence of the corrosion layer formed under dynamic conditions and its spallation (Fig. 6), a twofold increase of Cr content in the salt after the test suggests at least twofold increase of corrosion rate due to dynamic conditions. Magnesium and manganese are, respectively, a common impurity in molten salts and a component of SS310. Their concentration values are equivalent in both cases, considering the experimental uncertainty. Impurity of Al most probably arises from the alumina crucible used for the corrosion test. Ca is an impurity of the used salt, which reacts with SS310. In case of dynamic test, one expects more pronounced reaction, so lower concentration is evident after the corrosion tests (Table 3).

The variation of the main elements of the salt after the corrosion tests has also been analysed by XPS. In Fig. 11, the concentrations of the

elements are plotted for a pristine sample and the salts underwent dynamic and static experiments. Lithium concentration for the tested salts drops down to the detection limit of the technique. This behaviour is linked to the decomposition of Li_2CO_3 to form a mixed oxide of lithium and iron according to the reaction (1).

The reduction in the oxygen concentration is expected, since apart from air, the CO_3^{2-} ions are additional source of oxygen for the oxidation.

From the XPS analysis, one can also note that percentage of Na maintained similar to the pristine concentration, while K noticeably increased. The rise is lower for the static test, which can be attributed to the incorporation of potassium to the corrosion layer as K_2NiO_2 (Fig. 7).

Overall, it can be stated that the eutectic carbonate salt components interact with SS310 according to their reactivity as $\text{Li}_2\text{CO}_3 > \text{Na}_2\text{CO}_3 > \text{K}_2\text{CO}_3$. This fact has been confirmed by thermodynamic considerations [34]. The three components decompose to an alkali metal oxide according to the following reaction:



where A represents Li, Na or K. The activity of the alkali metal oxides calculated at 600 °C are 6.61×10^{-3} for Li_2CO_3 mol/L, 1.91×10^{-9} for Na_2CO_3 mol/L, and 1.208×10^{-13} for K_2CO_3 mol/L [34].

4. Conclusions

In this work, the influence of the dynamic conditions on the high temperature corrosion was analysed for SS310 stainless steel immersed in the eutectic ternary $\text{K}_2\text{CO}_3\text{-Na}_2\text{CO}_3\text{-Li}_2\text{CO}_3$ salt at 600 °C under air atmosphere. The dynamic conditions were realized by rotating the sample in the melted salt to simulate the flow of the molten salt in real working conditions. A static test was carried out as reference. The following conclusions can be inferred from this study:

1. Dynamic conditions greatly enhanced the corrosion of SS310 in molten ternary carbonate salt compared to the static case. This effect was evidenced by a much larger spallation of the corrosion layer in dynamic experiment, which produced a thinner and less protective corrosion layer.
2. ICP analysis of the salt after corrosion experiments confirmed at least twofold increase of Cr dissolution from SS310 into molten salt for dynamic conditions.
3. XPS characterization of the tested salts evidenced that the components of the ternary carbonate salt interacted with SS310 according to their reactivity: $\text{Li}_2\text{CO}_3 > \text{Na}_2\text{CO}_3 > \text{K}_2\text{CO}_3$.
4. XRD and SEM-EDX analysis revealed the corrosion products and their distribution within the corrosion layer (Fig. 8).
5. The comparison of the obtained corrosion rates with the previously published results suggests that steel-to-molten salt ratio can play an important role in the absolute values of the corrosion rate.

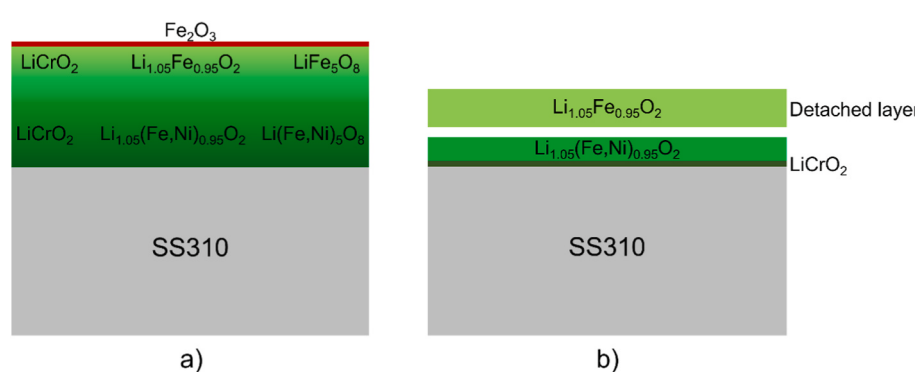


Fig. 9. Schematic representation of corrosion layer of SS310 after 600 h corrosion test at 600 °C under a) static conditions and b) dynamic conditions.

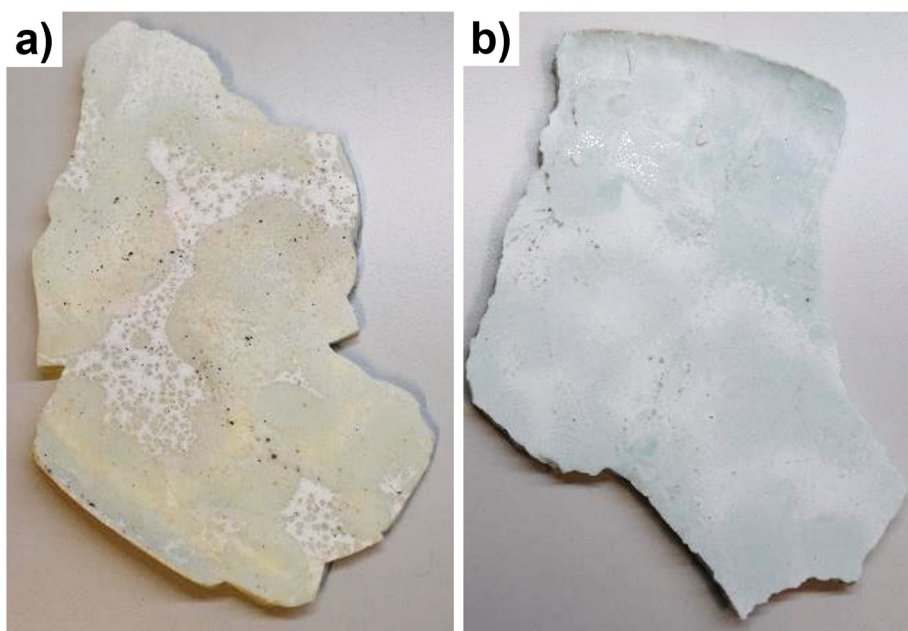


Fig. 10. Photos of the ternary carbonate salt after 600 h corrosion experiment with SS310 at 600 °C under a) static and b) dynamic conditions.

Table 3

Concentration of impurities in the salts after corrosion tests determined by ICP-OES.

Element	Cr (ppm)	Mg (ppm)	Mn (ppm)	Ca (ppm)	Al (ppm)
Dynamic test	1,560	0,752	0,080	0,481	0,271
Static test	0,617	0,712	0,103	1,103	0,0192

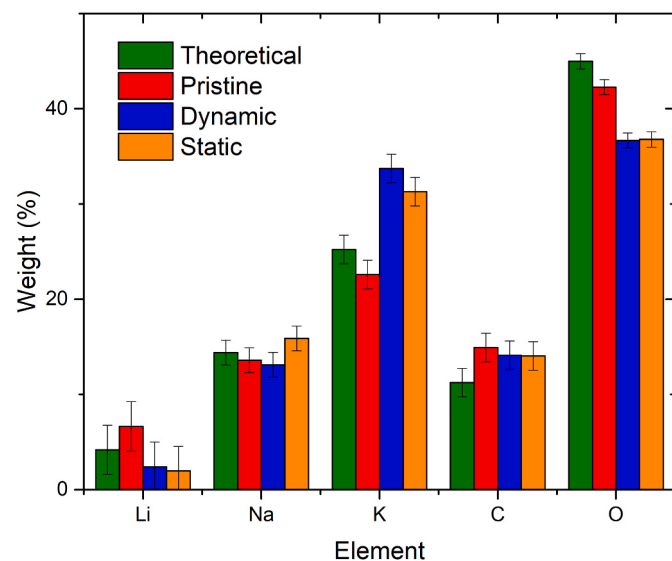


Fig. 11. Concentration of elements of the ternary carbonate salt: theoretical values and experimental data obtained by XPS for pristine and salts tested under dynamic and static conditions with SS310 at 600 °C for 600 h.

This study remarks that dynamic conditions have important effect on the corrosivity of the ternary molten carbonate salt. The most prominent discoveries are the significant spallation increase and the chromium dissolution enhancement compared to the experiments in static conditions. Considering this, it is clear that the results obtained in standard immersion tests cannot be trusted for assessing the performance of components in contact with pumped salt, such as pipes, valves, heat

exchangers, etc. Therefore, the results from dynamic corrosion experiments should be taken in special consideration in the design of the thermal energy storage unit for the 3rd generation concentrated solar power plants.

CRediT authorship contribution statement

Luis González-Fernández: Conceptualization, Methodology, Formal analysis, Investigation, Writing – original draft, preparation, Writing – review & editing, Supervision. **Mikel Intxaustieta-Carcedo:** Resources. **Oleksandr Bondarchuk:** Formal analysis, Investigation, Writing – review & editing. **Yaroslav Grosu:** Conceptualization, Methodology, Formal analysis, Writing – review & editing, Supervision, Project administration.

Declaration of competing interest

The authors declare that they have no known competing financial interests or personal relationships that could have appeared to influence the work reported in this paper.

Acknowledgements

The authors express their sincere thanks to Cristina Luengo and Yagmur Polat for their technical support, and to Diana Lopez for her assistance with ICP measurements.

References

- [1] M.T. Islam, N. Huda, A.B. Abdullah, R. Saidur, A comprehensive review of state-of-the-art concentrating solar power (CSP) technologies: current status and research trends, Renew. Sustain. Energy Rev. 91 (2018) 987–1018, <https://doi.org/10.1016/j.rser.2018.04.097>.
- [2] E. Zarza-Moya, A Comprehensive Guide to Solar Energy Systems, first ed., Academic Press, 2018.
- [3] M.H. Ahmadi, M. Ghazvini, M. Sadeghzadeh, M.A. Nazari, R. Kumar, A. Naeimi, T. Ming, Solar power technology for electricity generation: a critical review, Energy Sci. Eng. 6 (2018) 340–361, <https://doi.org/10.1002/ese3.239>.
- [4] C. Kost, S. Shammugam, V. Jülich, H. Nguyen, T. Schlegl, Levelized Cost of Electricity- Renewable Energy Technologies, Fraunhofer Institute for Solar Energy Systems, 2018.
- [5] M. Liu, N.H.S. Tay, S. Bell, M. Belusko, R. Jacob, G. Will, W. Saman, F. Bruno, Review on concentrating solar power plants and new developments in high

- temperature thermal energy storage technologies, *Renew. Sustain. Energy Rev.* 53 (2016) 1411–1432, <https://doi.org/10.1016/j.rser.2015.09.026>.
- [6] J. Lilliestam, T. Barradi, N. Caldés, M. Gomez, S. Hanger, J. Kern, N. Komendantova, M. Mehos, W.M. Hong, Z. Wang, A. Patt, Policies to keep and expand the option of concentrating solar power for dispatchable renewable electricity, *Energy Pol.* 116 (2018) 193–197, <https://doi.org/10.1016/j.enpol.2018.02.014>.
- [7] H. Zhang, J. Baeyens, G. Cáceres, J. Degrève, Y. Lv, Thermal energy storage: recent developments and practical aspects, *Prog. Energy Combust. Sci.* 53 (2016) 1–40, <https://doi.org/10.1016/j.jpecs.2015.10.003>.
- [8] A.G. Fernández, J. Gomez-Vidal, E. Oró, A. Kruizinga, A. Solé, L.F. Cabeza, Mainstreaming commercial CSP systems: a technology review, *Renew. Energy* 140 (2019) 152–176, <https://doi.org/10.1016/j.renene.2019.03.049>.
- [9] R.W. Bradshaw, Thermal convection loop study of the corrosion of incoloy 800 in molten NaNO₃-KNO₃, *Corrosion* 43 (1987) 173–178, <https://doi.org/10.5006/1.3583131>.
- [10] A.M. Kruizinga, D.D. Gill, M. LaFord, *Materials Corrosion of High Temperature Alloys Immersed in 600°C Binary Nitrate Salt*, SAND 2013-2526, 2013.
- [11] A.M. Kruizinga, D.D. Gill, M. LaFord, G. McConohy, *Corrosion of High Temperature Alloys in Solar Salt at 400, 500, and 680°C*, SAND 2013-8256, 2013.
- [12] P. Audigé, V. Encinas-Sánchez, M. Juez-Lorenzo, S. Rodríguez, M. Gutiérrez, F. J. Pérez, A. Agüero, High temperature molten salt corrosion behavior of aluminate and nickel-aluminate coatings for heat storage in concentrated solar power plants, *Surf. Coatings. Technol.* 349 (2018) 1148–1157, <https://doi.org/10.1016/j.surfcoat.2018.05.081>.
- [13] A. Bonk, D. Ruckle, S. Kaesche, M. Braun, T. Bauer, Impact of Solar Salt aging on corrosion of martensitic and austenitic steel for concentrating solar power plants, *Sol. Energy Mater. Sol. Cells* 203 (2019) 110162, <https://doi.org/10.1016/j.solmat.2019.110162>.
- [14] A. Gomes, M. Navas, N. Uranga, T. Paiva, I. Figueira, T.C. Diamantino, High-temperature corrosion performance of austenitic stainless steels type AISI 316L and AISI 321H, in molten Solar Salt, *Sol. Energy* 177 (2019) 408–419, <https://doi.org/10.1016/j.solener.2018.11.019>.
- [15] A.G. Fernández, L.F. Cabeza, Molten salt corrosion mechanisms of nitrate based thermal energy storage materials for concentrated solar power plants: a review, *Sol. Energy Mater. Sol. Cells* 194 (2019) 160–165, <https://doi.org/10.1016/j.j.solmat.2019.02.012>.
- [16] M. Mehos, C. Turchi, J. Vidal, M. Wagner, Z. Ma, C. Ho, W. Kolb, C. Andraka, A. Kruizinga, Concentrating solar power Gen3 demonstration roadmap, in: National Renewable Energy Lab. (NREL), Golden, CO (United States), 2017.
- [17] W. Ding, A. Bonk, T. Bauer, Corrosion behavior of metallic alloys in molten chloride salts for thermal energy storage in concentrated solar power plants: a review, *Front. Chem. Eng.* 12 (2018) 564–576, <https://doi.org/10.1007/s11705-018-1720-0>.
- [18] J.C. Vidal, N. Klammer, Molten chloride technology pathway to meet the U.S. DOE sunshot initiative with Gen3 CSP, *AIP Conf. Proc.* 2126 (2019), 080006, <https://doi.org/10.1063/1.5117601>.
- [19] W. Ding, J. Gomez-Vidal, A. Bonk, T. Bauer, Molten chloride salts for next generation CSP plants: electrolytical salt purification for reducing corrosive impurity level, *Sol. Energy Mater. Sol. Cells* 199 (2019) 8–15, <https://doi.org/10.1016/j.solmat.2019.04.021>.
- [20] R.I. Olivares, C. Chen, S. Wright, The thermal stability of molten lithium-sodium-potassium carbonate and the influence of additives on the melting point, *J. Sol. Energy Eng. Trans.* 134 (2012), 041002, <https://doi.org/10.1115/1.4006895>.
- [21] X. An, J. Cheng, P. Zhang, Z. Tang, J. Wang, Determination and evaluation of the thermophysical properties of an alkali carbonate eutectic molten salt, *Faraday Discuss.* 190 (2016) 327–338, <https://doi.org/10.1039/C5FD00236B>.
- [22] R. Raud, R. Jacob, F. Bruno, G. Will, T.A. Steinberg, A critical review of eutectic salt property prediction for latent heat energy storage systems, *Renew. Sustain. Energy Rev.* 70 (2017) 936–944, <https://doi.org/10.1016/j.rser.2016.11.274>.
- [23] C. Prieto, S. Fereres, F. JavierRuiz-Cabañas, A. Rodriguez-Sánchez, C. Montero, Carbonate molten salt solar thermal pilot facility: plant design, commissioning and operation up to 700 °C, *Renew. Energy* 151 (2020) 528–541, <https://doi.org/10.1016/j.renene.2019.11.045>.
- [24] T.-H. Lim, E.R. Hwang, H.Y. Ha, S.W. Nam, I.-H. Oh, S.-A. Hong, Effects of temperature and partial pressure of CO₂/O₂ on corrosion behaviour of stainless-steel in molten Li/Na carbonate salt, *J. Power Sources* 89 (2000) 1–6, [https://doi.org/10.1016/S0378-7753\(00\)00376-1](https://doi.org/10.1016/S0378-7753(00)00376-1).
- [25] S. Frangini, S. Loreti, The role of temperature on the corrosion and passivation of type 310S stainless steel in eutectic (Li₂K) carbonate melt, *J. Power Sources* 160 (2006) 800–804, <https://doi.org/10.1016/j.jpowsour.2006.04.068>.
- [26] K. Takeuchi, A. Nishijima, K. Ui, N. Koura, C.-K. Loong, Corrosion behavior of Fe-Cr alloys in Li₂CO₃-K₂CO₃ molten carbonate, *J. Electrochem. Soc.* 152 (2005) B364–B368, <https://doi.org/10.1149/1.1955168>.
- [27] M.T. de Miguel, V. Encinas-Sánchez, M.I. Lasanta, G. García-Martín, F.J. Pérez, Corrosion resistance of HR3C to a carbonate molten salt for energy storage applications in CSP plants, *Sol. Energy Mater. Sol. Cells* 157 (2016) 966–972, <https://doi.org/10.1016/j.solmat.2016.08.014>.
- [28] S.P. Sah, Corrosion of 304 stainless steel in carbonates melt– a state of enhanced dissolution of corrosion products, *Corrosion Sci.* 169 (2020) 108535, <https://doi.org/10.1016/j.corsci.2020.108535>.
- [29] A.G. Fernández, F. Pineda, M. Walczak, L.F. Cabeza, Corrosion evaluation of alumina-forming alloys in carbonate molten salt for CSP plants, *Renew. Energy* 140 (2019) 227–233, <https://doi.org/10.1016/j.renene.2019.03.087>.
- [30] M. Sarvghad, T.A. Steinberg, G. Will, Corrosion of stainless steel 316 in eutectic molten salts for thermal energy storage, *Sol. Energy* 172 (2018) 198–203, <https://doi.org/10.1016/j.solener.2018.03.053>.
- [31] M. Sarvghad, T.A. Steinberg, G. Will, Corrosion of steel alloys in eutectic NaCl + Na₂CO₃ at 700 °C and Li₂CO₃ + K₂CO₃ + Na₂CO₃ at 450 °C for thermal energy storage, *Sol. Energy Mater. Sol. Cell.* 170 (2017) 48–59, <https://doi.org/10.1016/j.solmat.2017.05.063>.
- [32] M. Sarvghad, O. Muransky, T.A. Steinberg, J. Hester, M.R. Hill, G. Will, On the effect of cold-rolling on the corrosion of SS316L alloy in a molten carbonate salt, *Sol. Energy Mater. Sol. Cell.* 202 (2019) 110136, <https://doi.org/10.1016/j.solmat.2019.110136>.
- [33] M. Saryghad, T. Chenu, G. Will, Comparative interaction of cold-worked versus annealed inconel 601 with molten carbonate salt at 450 °C, *Corrosion Sci.* 116 (2017) 88–97, <https://doi.org/10.1016/j.corsci.2017.01.004>.
- [34] J. Luo, C.K. Deng, N.H. Tariq, N. Li, R.F. Han, H.H. Liu, J.Q. Wang, X.Y. Cui, T. Y. Xiong, Corrosion behavior of SS316L in ternary Li₂CO₃-Na₂CO₃-K₂CO₃ eutectic mixture salt for concentrated solar power plants, *Sol. Energy Mater. Sol. Cells* 217 (2020) 110679, <https://doi.org/10.1016/j.solmat.2020.110679>.
- [35] Y. Grosu, A. Anagnostopoulos, B. Balakin, J. Krupanek, M.E. Navarro, L. González-Fernández, Y. Ding, A. Faik, Nanofluids based on molten carbonate salts for high-temperature thermal energy storage: thermophysical properties, stability, compatibility and life cycle analysis, *Sol. Energy Mater. Sol. Cells* 220 (2021) 110838, <https://doi.org/10.1016/j.solmat.2020.110838>.
- [36] Y. Grosu, A. Anagnostopoulos, M.E. Navarro, Y. Ding, A. Faik, Inhibiting hot corrosion of molten Li₂CO₃-Na₂CO₃-K₂CO₃ salt through graphitization of construction materials for concentrated solar power, *Sol. Energy Mater. Sol. Cells* 215 (2020) 110650, <https://doi.org/10.1016/j.solmat.2020.110650>.
- [37] G. García-Martín, M.I. Lasanta, V. Encinas-Sánchez, M.T. de Miguel, F.J. Pérez, Evaluation of corrosion resistance of A516 Steel in a molten nitrate salt mixture using a pilot plant facility for application in CSP plants, *Sol. Energy Mater. Sol. Cells* 161 (2017) 226–231, <https://doi.org/10.1016/j.solmat.2016.12.002>.
- [38] J. Nieto-Maestre, B. Muñoz-Sánchez, A.G. Fernández, A. Faik, Y. Grosu, A. García-Romero, Compatibility of container materials for Concentrated Solar Power with a solar salt and alumina based nanofluid: a study under dynamic conditions, *Renew. Energy* 146 (2020) 384–396, <https://doi.org/10.1016/j.renene.2019.06.145>.
- [39] X. Zhang, C. Zhang, Y. Wu, Y. Lu, Experimental research of high temperature dynamic corrosion characteristic of stainless steels in nitrate eutectic molten salt, *Sol. Energy* 209 (2020) 618–627, <https://doi.org/10.1016/j.solener.2020.09.034>.
- [40] J. Wang, Y. Jiang, Y. Ni, A. Wu, J. Li, Investigation on static and dynamic corrosion behaviors of thermal energy transfer and storage system materials by molten salts in concentrating solar power plants, *Mater. Corros.* 70 (2018) 102–109, <https://doi.org/10.1002/maco.201810362>.
- [41] P. Che, F. Wang, M. Xie, Q. Li, Y. Zhang, Y. Cheng, Corrosion behavior research on austenitic stainless steel in dynamic molten salt, *J. Phys.: Conf. Ser.* 2085 (2021), 012025, <https://doi.org/10.1088/1742-6596/2085/1/012025>.
- [42] F. Sutter, C. Oskay, M.C. Galetz, T. Diamantino, F. Pedrosa, I. Figueira, S. Glumm, A. Bonk, A. Agüero, S. Rodríguez, T.J. Reche-Navarro, S. Caron, Dynamic corrosion testing of metals in solar salt for concentrated solar power, *Sol. Energy Mater. Sol. Cells* 232 (2021) 111331, <https://doi.org/10.1016/j.solmat.2021.111331>.
- [43] A.G. Fernández, B. Muñoz-Sánchez, J. Nieto-Maestre, L.F. Cabeza, Dynamic corrosion test using LiNO₃ containing molten salt for CSP applications, *Appl. Sci.* 10 (2020) 4305, <https://doi.org/10.3390/app10124305>.
- [44] L. Ma, C. Zhang, Y. Wu, Y. Lu, C. Ma, Dynamic corrosion behavior of 316L stainless steel in quaternary nitrate-nitrite salts under different flow rates, *Sol. Energy Mater. Sol. Cells* 218 (2020) 110821, <https://doi.org/10.1016/j.solmat.2020.110821>.
- [45] P. Audigé, V. Encinas-Sánchez, S. Rodríguez, F.J. Pérez, A. Agüero, High temperature corrosion beneath carbonate melts of aluminate coatings for CSP application, *Sol. Energy Mater. Sol. Cells* 210 (2020) 110514, <https://doi.org/10.1016/j.solmat.2020.110514>.
- [46] K. Lippiatt, S. Bell, T.-C. Ong, C. East, D. McAuley, G. Will, T. Steinberg, An improved technique for molten salt corrosion sample preparation, *Sol. Energy Mater. Sol. Cells* 226 (2021) 111057, <https://doi.org/10.1016/j.solmat.2021.111057>.